optica

Excitonic gain and laser emission from mixed-cation halide perovskite thin films: supplementary material

SONGTAO CHEN[1] AND ARTO NURMIKKO[1,2,*]

[1]School of Engineering, Brown University, Providence, Rhode Island 02912

[2]Department of Physics, Brown University, Providence, Rhode Island 02912

*Corresponding author: arto_nurmikko@brown.edu

Published 20 September 2018

This document provides supplementary information to "Excitonic gain and laser emission from mixed-cation halide perovskite thin films," https://doi.org/10.1364/OPTICA.5.001141.

1. DETAILS OF FABRICATION PROCESS OF MIXED-CATION $CS_{0.17}FA_{0.83}PbBr_3$ PEROVSKITE THIN FILMS

Lead bromide ($PbBr_2$, 99.999%) and cesium bromide (CsBr, 99.999%) were purchased from Alfa Aesar. Anhydrous dimethyl sulfoxide (DMSO) (99.9%) was purchased from Sigma Aldrich. Formamidinium bromide (FABr, > 98%) was purchased from Dyesol. All the materials were used as received. In a N_2 atmosphere glove box (with H_2O < 0.1 ppm and O_2 < 0.1 ppm), we mixed CsBr, FABr, and $PbBr_2$ with molar ratio = 0.17:0.83:1 into anhydrous DMSO for a 25 wt% solution which was stirred until all the precursors were dissolved in host solvent. A 0.45 μm PVDF filter was used to eliminate impurities in the solution. A 15 μL mixed precursor solution was spread onto clean quartz or DBR surface (which were treated before use by oxygen plasma to create hydrophilic surface) and spin-cast at 2000 rpm for 63 s. During the spin-casting, 50 μL toluene was quickly dripped vertically targeting the center of the sample at 50 s after start of spin-casting. Then the film was transferred onto a hotplate (80 °C) for 5 mins annealing, which facilitated the crystal growth to form the final mixed-cation perovskite ($Cs_{0.17}FA_{0.83}PbBr_3$) thin film. The fabricated fresh films were then used for further

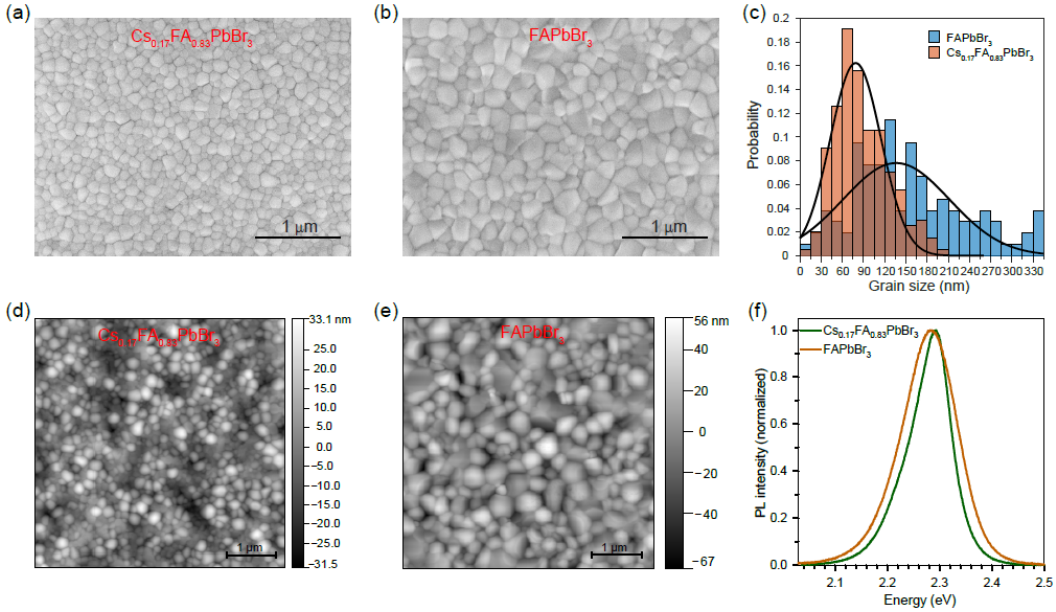

Fig. S1. SEM images of surface morphology of (a) $Cs_{0.17}FA_{0.83}PbBr_3$ and (b) $FAPbBr_3$ thin films. (c) Grain size distribution of two types of films, showing the mixed-cation perovskite film has both smaller grain size and narrower size distribution than the pure-cation film. Black lines are the Gaussian profile fitting. AFM surface profiles of (d) $Cs_{0.17}FA_{0.83}PbBr_3$ and (e) $FAPbBr_3$ thin films, with RMS roughness of 9.7 nm and 17.5 nm, respectively. (f) PL spectrum comparison between the two types of films, where mixed-cation perovskite films show slightly higher energy peak and narrower FWHM linewidth.

characterizations. Pure-cation non-cesium perovskite ($FAPbBr_3$) thin films were also fabricated by the same method for making comparisons between the two types.

For completing full PeVCSEL devices, after fabricating of the mixed-cation perovskite ($Cs_{0.17}FA_{0.83}PbBr_3$) thin film on the surface of bottom DBR, we speedily moved the samples back into the sputtering chamber (with very limited exposure in the ambient environment). We waited until the sputtering chamber pressure reached ~ 10^{-8} Torr to ensure minimal residue of oxygen or water molecules on the perovskite thin film surface before we started to sputter the top DBR (same recipe/parameters as bottom DBR). Given the lower index and better adhesion of SiO_2 layer to the perovskite film, we designed both the bottom and top DBRs so that each surface of the perovskite thin film contacted with SiO_2 layer. Reference quartz substrates were also coated with DBR for measuring the reflectivity spectrum.

2. COMPARISONS WITH PURE-CATION $FAPbBr_3$ PEROVSKITE THIN FILMS

After adding judicious amount of the cesium component, the mixed-cation perovskites showed improved structural and optical properties, with results summarized in Fig. S1. The grain size distribution was extracted from the surface morphology SEM images from the two films (Fig. S1(a) and Fig. S1(b)). As shown in Fig. S1(c), $Cs_{0.17}FA_{0.83}PbBr_3$ films exhibit not only smaller grain sizes, but the size distribution is also narrower than $FAPbBr_3$ films. By using an approximate Gaussian distribution fitting $f(\mu,\sigma)$ where μ is the mean value and σ is the standard deviation, we can quantitatively define the grain size distribution as μ = 79 nm, σ = 51 nm and μ = 136 nm, σ = 107 nm for $Cs_{0.17}FA_{0.83}PbBr_3$ and $FAPbBr_3$ films, respectively. With smaller grain sizes, $Cs_{0.17}FA_{0.83}PbBr_3$ films also show less surface roughness (RMS ~ 9.7 nm) than $FAPbBr_3$ films (RMS ~ 17.5 nm), as shown in Fig. S1(d) and Fig. S1(e). The smoother film will help to lower the scattering loss which thus decreases the threshold gain of related PeVCSEL devices. Meanwhile the narrower distribution leads to less inhomogeneous broadening. It is reflected as narrower PL FWHM linewidth as plotted in Fig. S1(f). Mixed-cation $Cs_{0.17}FA_{0.83}PbBr_3$ films have a PL spectrum peaked at 2.289 eV with FWHM linewidth of 80.4 meV, while those of $FAPbBr_3$ films are 2.282 eV and 111.7 meV, respectively. The detail physical mechanism of why adding cesium within a limited composition range ($x \approx 0.17$) can significantly help in improving the perovskite's structural and optical properties is not yet clear from the literature nor to us, and needs further experimental and electronic structure analysis.

For modeling of the near band edge absorption spectrum to extract exciton binding energy, the equation (1) in the main text can be rewritten as equation (S1),

$$\alpha(\hbar\omega) = \frac{A}{\hbar\omega}\left[2E_b \operatorname{sech}\left(\frac{\hbar\omega - E_g + E_b}{\Gamma}\right) + \int_{E_g}^{\infty} \operatorname{sech}\left(\frac{\hbar\omega - E}{\Gamma}\right) \frac{1}{1 - e^{-2\pi\sqrt{E_b/(E-E_g)}}} dE\right] \quad \text{(S1)}$$

where the transition dipole moment square and $2\pi\sqrt{E_b}$ have been absorbed into the proportionality factor A, which has the dimension of cm^{-1}. In the fitting results shown in Fig. 3(c) in the main text, the proportionality factor A equals 1.046×10^6 cm^{-1}.

3. VOIGT PROFILE FITTING AND LO PHONON ENERGIES

Beyond the method used in the main text by fitting the PL FWHM linewidth (contribution by Fröhlich interaction) at different temperatures to extract the LO phonon energy, the PL spectrum at low temperature also contains information about electron – LO phonon coupling. At T = 10 K, the PL spectrum shows different bands (Fig. S2) correspond to the radiative recombination with zero, one or more participating phonons. Electron-phonon coupling *via* the Fröhlich interaction involves releasing excess energy to the lattice vibrations as LO phonons, which is observable as one or more evenly spaced phonon side bands on the low energy side of PL spectrum. At higher temperatures, this feature is difficult to isolate due to thermal contributions to the process and line broadening. Here, for the mixed-cation $Cs_{0.17}FA_{0.83}PbBr_3$ we observed two PL bands at T = 10 K, the

Perovskites	Γ_{inh} (meV)	Γ_{LO} (meV)	$\hbar\omega_{LO}$ (meV)	Reference
$FAPbBr_3$	20 ± 1	61 ± 7	15.3 ± 1.4	2
$MAPbBr_3$	32 ± 2	58 ± 2	15.3	2
$FAPbI_3$	19 ± 1	40 ± 5	11.5 ± 1.2	2
$MAPbI_3$	26 ± 2	40 ± 2	11.5	2
$MAPbI_{3-x}Cl_x$	38.0 ± 3.7	92.1 ± 23.5	25.3 ± 5.2	3
$MAPbCl_3$	n.a	n.a	27.9	4
$MAPbBr_3$	n.a	n.a	20.7	4
$MAPbI_3$	n.a	n.a	16.4	4
$CsPbCl_3$ SC	n.a	n.a	43/46.9	5/6
$CsPbBr_3$ SC	n.a	n.a	47.3	7
$CsPbCl_3$ NCs	67.2 ± 0.3	87.0 ± 14.9	42.8 ± 4.5	8
$CsPbBr_3$ NCs	40.0 ± 0.5	86.7 ± 31.4	44.4 ± 10.2	8
$CsPbI_3$ NCs	52.1 ± 0.7	46.1 ± 11.1	26.3 ± 7.0	8
$Cs_{0.17}FA_{0.83}PbBr_3$	**32.7 ± 0.4**	**93.3 ± 10.1**	**28.7 ± 1.9**	**our work**

Table. S1. Comparison of extracted LO phonon energies from multiple literature sources; citations refer to reference numbers at the end of this Supplement. Abbreviations: SC: single crystal; NCs: nanocrystals; other non-specified are thin film samples.

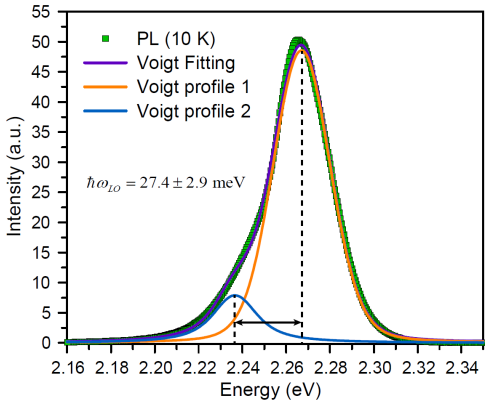

Fig. S2. Low temperature (T = 10 K) PL spectrum fitting by sum of two Voigt profiles to resolve the zero-phonon and one-phonon side bands. The energy difference between these two bands is used to extract the LO-phonon energy as shown in the figure.

separation of which approximates the LO phonon energy [1]. Voigt profiles were used to fit the PL spectrum of $Cs_{0.17}FA_{0.83}PbBr_3$ films at T = 10 K. The Voigt profile consists of convolution of Gaussian and Lorenztian profiles, which accounts for both the homogeneous and inhomogeneous broadening mechanisms. As shown in Fig. S2, this Voigt profile can well fit the PL spectrum, yielding two PL bands separating from each other by 27.4 ± 2.9 meV – i.e. the LO phonon energy. This value matches the LO phonon energy (28.7 ± 1.9 meV) obtained by fitting the PL spectrum linewidth change at variable temperatures. Table S1 summarizes the LO phonon energies reported in the literature for different kinds of perovskite materials. We find our values qualitatively matching those in the literature within the large range of energies reported. Both the material form of a perovskite sample (e.g. single crystal, nanocrystal or polycrystalline thin film) and its fabrication methods might affect the microscopic details of the perovskite crystals, leading to rather different phonon energies.

4. Ultrafast time-resolved pump-probe experiments

To verify excitons' persistence at high carrier density ($\rho \sim 10^{18}$ cm^{-3}) and their capability to create excitonic optical gain, we conducted the time-resolved transient absorption measurements through a standard pump-probe setup as shown in Fig. S3. Starting from an ultrafast (1.55 eV, τ_{pulse} = 100 fs, 100 kHz) Ti:Sapphire laser, we used the second harmonic generation output (3.1 eV, τ_{pulse} = 100 fs, 100 kHz) of the Ti:Sapphire as the pump beam, while another portion of Ti:Sapphire laser was focused into a (χ^3) nonlinear crystal to generate super-continuum white light by self-phase modulation. The white light traveled through a variable delay stage to adjust the arrival time difference (Δt) against pump beam. This Δt could be tuned from -100 ps to 1200 ps in the current setup. The super-continuum white light then passed through a monochromator to pick specific wavelength as the probe beam. Fine tuning of the mirror that reflects the super-continuum

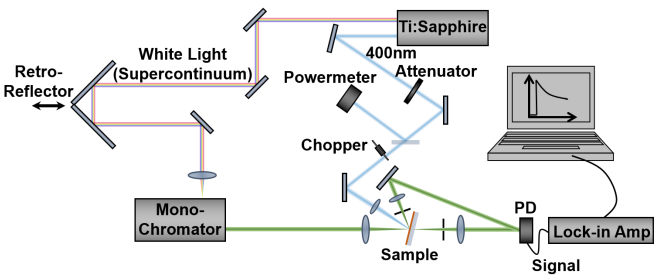

Fig. S3. Schematic time-resolved pump-probe setup for measuring the gain spectroscopy for mixed-cation $Cs_{0.17}FA_{0.83}PbBr_3$ perovskite thin films. PD: photodetector; Lock-in Amp: lock-in amplifier. Components like mirrors, lenses and pinholes are represented as normal geometries.

light into the retroreflector is required to avoid the beam walk issue when delay stage moves. Both the pump beam and the probe beam were focused onto the sample by focusing lenses, with probe beam spot locating at the center of the pump beam spot ($r_{pump} \approx 3\, r_{probe}$). The mixed-cation perovskite thin film sample (d = 239.5 ± 9.7 nm) was mounted to make probe beam incidence angle to be 10°, so that both the reflected and transmitted probe beams could be collected into the photodetector that was connected to a lock-in amplifier for calculating the accurate absorption values. For pump-modulated nonlinear absorption measurements, an optical chopper was used in the pathway of pump beam and the chopper frequency (3 kHz, phase-locked) was feed into the lock-in amplifier for data acquisition. The strong PL emission under the excitations by pump beam can be the noise source for transient absorption measurements. To decrease the influence of PL emission, we used two pinholes (one on reflection side, another one on transmission side) to block the PL emission as much as possible.

5. Absorption cross section and oscillator strength

The excitonic feature of mixed-cation $Cs_{0.17}FA_{0.83}PbBr_3$ in the absorption can benefit the material to have enhanced excitonic absorption below the bandgap with more concentrated oscillator strength in a narrow spectral window (FWHM of 68.5 meV for mixed-cation perovskite thin films). To estimate the absorption cross section σ_{abs} at excitonic transition, we used the relation of $\sigma_{abs} = \alpha/\rho$, where α is the absorption coefficient (in unit of cm^{-1}) at excitonic peak and ρ is the exciton density (in unit of cm^{-3}). Different from the case such as absorbing molecules in solution, where ρ is replaced by the molecule volume concentration *N*, here we approximately take the density of absorbing entities as the concentration of excitons [9] for the bulk-like perovskite thin films. For example, when optical gain first onsets (i.e. system just reaches the population inversion condition) under carrier density $\rho = 6.51 \times 10^{17}$ cm^{-3}, the absorption cross section $\sigma_{abs} = \alpha/\rho = 6.47 \times 10^{-14}$ cm^2. This estimated number matches other reported absorption cross section values for perovskite materials [10, 11], while it's about one order magnitude larger than II-VI CdSe based nanocrystals [12, 13].

Another fundamentally important parameter that measures the strength of optical transitions is the oscillator strength. To estimate the oscillator strength *f*, we used the following equation [9],

$$Nf = \frac{4m_0\varepsilon_0 cn}{e^2 h}\int \alpha(E)dE \qquad \text{(S2)}$$

where $\alpha(E)$ is the excitonic absorption coefficient (see brown solid line in main text Fig. 3(c)); *E* is the photon energy; *n* is the refractive index; m_0, ε_0, *c*, *e*, *h* are fundamental physical constants: electron mass, dielectric constant in vacuum, speed of light, element charge and Planck constant, respectively. Depending on how one defines absorbing entities, *N* can be the concentration of excitons or number of unit cells per unit volume. By using *N* as the exciton density with the same value for estimating the absorption cross section (see above), we have calculated the oscillator strength *f* = 122.7. This value is larger than excitonic semiconductors like GaAs [9] and II-VI CdSe based nanocrystals [14, 15], while it is smaller than perovskite materials with reduced dimensionality such as $CsPbBr_3$ nanoplatelets [16].

6. ASE EMISSION BY RESONANT PUMPING

For testing the ASE from mixed-cation $Cs_{0.17}FA_{0.83}PbBr_3$ films, we conducted the standard stripe excitation experiments, where the cylindrical lens was used to focus the input pump beam into a thin stripe (~ 15 μm × 1000 μm) on the perovskite thin film sample. The sample was cleaved at the center before testing to avoid edge effects and the ASE was collected by an objective lens from the side to the spectrometer. The $Cs_{0.17}FA_{0.83}PbBr_3$ films have a room temperature excitonic peak at 2.337 eV, which coincidentally matches the readily available diode-pump solid state laser at 2.331 eV (λ = 532 nm). We used this sub-ns

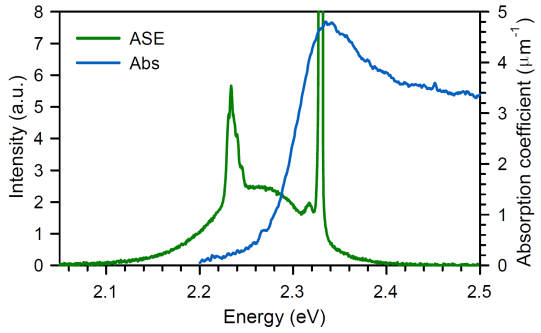

Fig. S4. ASE spectrum obtained from mixed-cation $Cs_{0.17}FA_{0.83}PbBr_3$ films under resonant pumping (2.331 eV, τ_{pulse} = 0.34 ns, 1 kHz) condition. The strong peak in the emission spectrum (green line) is the scattered pump laser that detected by spectrometer. Absorption spectrum (blue curve) is also plotted to illustrate the resonant pumping condition.

(τ_{pulse} = 0.34 ns, 1 kHz) laser source to resonantly pump the perovskite thin films and observed clear ASE signal (with ASE peak at 2.237 eV), as shown in Fig. S4. Due to the scattering, we also collected pump laser light residues which resulted in a strong and sharp artefact peak in the spectrum. Recall that the electron hole plasma continuum is 43.8 meV higher than the exciton band while the single LO phonon energy is insufficient to dissociate an exciton into a free electron-hole pair by the inelastic scattering process, therefore the observation of ASE spectrum under resonant pumping explicitly supports the argument for excitonic gain. This robust excitonic gain was exploited in the thin film based PeVCSEL devices as elaborated in the main text. Though resonant pumping is not compatible in VCSEL configuration, it can be easily applied in DFB grating or photonic crystal cavities where the in-plane feedback is exploited. By using the resonant ("cold photon") pumping, the energy difference between the pump photons and perovskite lasing photons (2.331 eV and 2.244 eV, respectively, 0.087 eV difference) will be much smaller than those used in current PeVCSEL cases (3.493 eV and 2.244 eV, respectively, 1.249 eV difference). Thus, the excess energy from the pump photons will be smaller which in turn introduces less thermal load onto the perovskite films in the resonant pumping case. Together with high thermal conductivity substrate such as MgF_2 [17,18], it might be possible to achieve CW lasing operation from perovskite materials at room temperature, though the in-plane scattering loss might also raise the lasing thresholds of these devices.

References

1. C. M. Iaru, J. J. Geuchies, P. M. Koenraad, D. Vanmaekelbergh, and A. Y. Silov, "Strong carrier-phonon coupling in lead halide perovskite nanocrystals," ACS Nano **11**, 11024-11030 (2017).
2. A. D. Wright, C. Verdi, R. L. Milot, G. E. Eperon, M. A. Perez-Osorio, H. J. Snaith, F. Giustino, M. B. Johnston, and L. M. Herz, "Electron-phonon coupling in hybrid lead halide perovskites," Nat. Commun. **7**, 11755 (2016).
3. K. Wu, A. Bera, C. Ma, Y. Du, Y, Yang, L. Li, and T. Wu, "Temperature-dependent excitonic photoluminescence of hybrid organometal halide perovskite films," Phys. Chem. Chem. Phys. **16**, 22476-22481 (2014).
4. M. Sendner, P. K. Nayak, D. A. Egger, S. Beck, C. Muller, B. Epding, W. Kowalsky, L. Kronik, H. J. Snaith, A. Pucci, and R. Lovrincic, "Optical phonons in methylammonium lead halide perovskites and implications for charge transport," Mater. Horiz. **3**, 613-620 (2016).
5. M. Sebastian, J. A. Peters, C. C. Stoumpos, J. Im, S. S. Kostina, Z. Liu, M. G. Kanatzidis, A. J. Freeman, and B. W. Wessels, "Excitonic emissions and above-band-gap luminescence in the single-crystal perovskite semiconductors $CsPbBr_3$ and $CsPbCl_3$," Phys. Rev. B **92**, 235210 (2015).
6. D. M. Calistru, "Identification of the symmetry of phonon modes in $CsPbCl_3$ in phase IV by Raman and resonance-Raman scattering," J. Appl. Phys. **82**, 5391 (1997).
7. J. Tilchin, D. N. Dirin, G. I. Maikov, A. Sashchiuk, M. V. Kovalenko, and E. Lifshitz, "Hydrogen-like Wannier-Mott excitons in single crystal of methylammonium lead bromide perovskite," ACS Nano **10**, 6363-6371 (2016).
8. R. Saran, A. H. Jungemann, A. G. Kanaras, and R. J. Curry, "Giant bandgap renormalization and exciton-phonon scattering in perovskite nanocrystals," Adv. Opt. Mater. **5**, 1700231 (2017).
9. G. W. Hooft, W. A. J. A. van der Poel, and L. W. Molenkamp, "Giant oscillator strength of free excitons in GaAs," Phys. Rev. B **35**, 8281-8284 (1987).
10. S. Yakunin, L. Protesescu, F. Krieg, M. I. Bodnarchuk, G. Nedelcu, M. Humer, G. D. Luca, M. Fiebig, W. Heiss, and M. V. Kovalenko, "Low-threshold amplified spontaneous emission and lasing from colloidal nanocrystals of caesium lead halide perovskites," Nat. Commun. **6**, 8056 (2015).
11. J. Chen, K. Zidek, P. Chabera, D. Liu, P. Cheng, L. Nuuttila, M. J. Al-Marri, H. Lehtivuori, M. E. Messing, K. Han, K. Zheng, and T. Pullerits, "Size- and wavelength-dependent two-photon absorption cross-section of $CsPbBr_3$ perovskite quantum dots," J. Phys. Chem. Lett. **8**, 2316-2321 (2017).
12. C. A. Leatherdale, W. K. Woo, F. V. Mikulec, and M. G. Bawendi, "On the absorption cross section of CdSe nanocrystal quantum dots," J. Phys. Chem. B **106**, 7619-7622 (2002).
13. J. Nanda, S. A. Ivanov, H. Htoon, I. Bezel, A. Piryatinski, S. Tretiak, and V. I. Klimov, "Absorption cross sections and Auger recombination lifetimes in inverted core-shell nanocrystals: Implications for lasing performance," J. Appl. Phys. **99**, 034309 (2006).
14. M. D. Leistikow, J. Johansen, A. J. Kettelarij, P. Lodahl, and W. L. Vos, "Size-dependent oscillator strength and quantum efficiency of CdSe quantum dots controlled via the local density of states," Phys. Rev. B **79**, 045301 (2009).
15. I. Angeloni, W. Raja, A. Polovitsyn, F. De Donato, R. P. Zaccaria, and I. Moreels, "Band-edge oscillator strength of colloidal CdSe/CdS dot-in-rods: Comparison of absorption and time-resolved fluorescence spectroscopy," Nanoscale **9**, 4730-4738 (2017).
16. J. Li, L. Luo, H. Huang, C. Ma, Z. Ye, J. Zeng, and H. He, "2D behaviors of excitons in cesium lead halide perovskite nanoplatelets," J. Phys. Chem. Lett. **8**, 1161-1168 (2017).
17. M. M. Adachi, F. Fan, D. P. Sellan, S. Hoogland, O. Voznyy, A. J. Houtepen, K. D. Parrish, P. Kanjanaboos, J. A. Malen, and E. H. Sargent, "Microsecond-sustained lasing from colloidal quantum dot solids," Nat. Commun. **6**, 8694 (2015).
18. F. Fan, O. Voznyy, R. P. Sabatini, K. T. Bicanic, M. M. Adachi, J. R. Mcbride, K. R. Reid, Y.S. Park, X. Li, A. Jain, P. Quintero, M. Saravanapavanantham, M. Liu, M. Korkusinski, P. Hawrylak, V. I. Klimov, S. J. Rosenthal, S. Hoogland, and E. H. Sargent, "Continuous-wave lasing in colloidal quantum dot solids enabled by facet-selective epitaxy," **544**, 75-79 (2017).